Quantifying microseismic noise generation from coastal reflection of gravity waves recorded by seafloor DAS

G. Guerin,[1] D. Rivet,[1] M. P. A. van den Ende [ORCID],[1] E. Stutzmann,[2] A. Sladen[1] and J.-P. Ampuero [ORCID][1]

[1]*Université Côte d'Azur, CNRS, Observatoire de la Côte d'Azur, IRD, Géoazur, Sophia Antipolis,* 06560 *Valbonne, France.*
E-mail: *gauthier.guerin@geoazur.unice.fr*
[2]*Institut de Physique du Globe de Paris, CNRS, Université de Paris, Paris, France*

SUMMARY

Secondary microseisms are the most energetic noise in continuous seismometer recordings. They are generated by interactions between ocean waves, including between gravity waves incident on and reflected from the coast. Coastal reflections of ocean waves leading to coastal microseismic sources are hard to estimate in various global numerical wave models, and independent quantification of these coastal sources through direct measurements can greatly improve these models. Here, we exploit a 41-km-long submarine optical fibre (OF) cable located offshore Toulon, France, using distributed acoustic sensing (DAS). We record both the amplitude and frequency of seafloor strains induced by ocean surface gravity waves, as well as secondary microseisms caused by the interaction of gravity waves incident and reflected from the coast. By leveraging the spatially distributed nature of DAS measurements, additional fundamental information is recovered such as the velocity and azimuth of the waves. We find that on average 30 per cent of the gravity waves are reflected at the coast generating local sources of secondary microseisms that manifest as Scholte waves. These local sources represent the most energetic contribution to the seismic noise recorded along the OF and by an onshore broad-band station located near the DAS interrogator. Furthermore, we estimate a coastal reflection coefficient of ocean surface gravity waves R^2 of about 0.07, which provides improved constraints for seismic noise generation models. In addition, we show that new local sources of microseisms can be generated when gravity waves characteristics (azimuth and frequency content) change and lead to some delays between the OF cable and buoy recordings. These analyses pave the way for a wide use of DAS data to monitor ocean–solid earth interactions as they provide a wealth of information on the reflection of gravity waves, coastal microseismic sources, and new constraints for numerical models of microseismic noise.

Key words: Seismic noise; Wave propagation; Interface waves.

1 INTRODUCTION

Oceanic gravity waves generate the most energetic contribution to the background seismic noise known as the primary and secondary microseisms, which are recorded worldwide by broad-band seismometers (Webb 1998; Stutzmann *et al.* 2000, 2001), and more recently also by optical fibre (OF) cables through distributed acoustic sensing (DAS, Sladen *et al.* 2019; Williams *et al.* 2019). The prevailing theory of microseism generation was initially developed by Longuet-Higgins (1950) and Hasselmann (1963). Primary microseisms arise from interactions between ocean swell and near-coastal bathymetry at shallow depths (less than 100 m depth) and generate excitations by shear traction at the seafloor dominated by Love waves (Nishida 2017). The resulting

wave periods range from 10 to 20 s (Hasselmann 1963; Cessaro 1994). Secondary microseisms are caused by the interference between opposing ocean surface gravity waves with equal frequencies, such as those generated by storms, or by the reflection of ocean waves on the coast (Ardhuin *et al.* 2012), which produce second-order pressure fluctuations close to the ocean surface at twice the frequency of the causative ocean surface gravity waves (Longuet-Higgins 1950; Hasselmann 1963). Microseismic sources generate hydro-acoustic waves in the ocean that are multiply reflected and transmitted at the ocean bottom, leading to microseism records dominated by Rayleigh waves (Bonnefoy-Claudet *et al.* 2006; Kedar *et al.* 2008; Stutzmann *et al.* 2009; Koper *et al.* 2010; Ardhuin *et al.* 2011; Stutzmann *et al.* 2012; Gualtieri *et al.* 2013).

Many studies have shown and quantified that the strongest secondary microseismic sources originate through storms from the deep ocean (Longuet-Higgins 1950; Stehly *et al.* 2006; Stutzmann *et al.* 2012), but few have been able to quantify the abundant smaller sources produced by the reflection of gravity waves on the coast (Bromirski & Duennebier 2002; Ardhuin *et al.* 2012), since offshore measurements are scarce. Moreover, coastal reflection sources may be overwhelmed by deep ocean sources.

Microseism source models are developed to provide a better understanding of the different classes of sources for oceanographic applications, as well as to provide information for seismic studies. Most models either do not include coastal reflection sources (Kedar *et al.* 2008) or use an approximate coefficient R^2 to quantify reflection at a global scale (Ardhuin *et al.* 2011). Stutzmann *et al.* (2012) used empirical values of R^2 in their model ranging from 1 to 20 per cent as a function of the coastal environment (continents, islands, or sea ice). Ardhuin *et al.* (2012) showed that the geometry of the coast (slope) may have a significant impact on coastal reflection recordings, particularly along steep bathymetry coastlines. Here we show that seafloor DAS measurements can improve the accuracy of microseism source models by providing a direct measurement of the ocean wave coastal reflection coefficient and a wealth of information on coastal microseism sources.

Seafloor DAS is an emerging technology in marine geophysics that exploits existing submarine fibre-optic telecommunication cables to fill the observational gaps in the oceans, including those that limit the study of near-shore microseisms (e.g. Sladen *et al.* 2019; Lindsey *et al.* 2019; Williams *et al.* 2019). DAS can convert a fibre optic cable of up to about 150 km length into a dense array of single-component (longitudinal) strain (or strain-rate) sensors, spaced merely a few meters apart and with temporal sampling rate up to several kHz. The submarine target environment can be sensed directly from land by connecting the DAS interrogator to one terrestrial end of the cable. The high density of seafloor measurements provided by DAS over a large area, combined with the ease of operation, revolutionize the measurement of transient ground deformations offshore. Microseismic noise is ubiquitous in underwater DAS continuous records (Sladen *et al.* 2019; Lindsey *et al.* 2019; Williams *et al.* 2019). Sladen *et al.* (2019) used an underwater cable located in the Mediterranean Sea and showed that seismic noise recorded at depths greater than 1000 m is dominated by Scholte waves in the frequency band 0.2–0.5 Hz. They also demonstrated that the DAS recordings close to shore had a dominant frequency of around 0.1 Hz produced by the pressure variations induced by the ocean surface gravity waves. Microseismic waves have also been recorded on submarine cables in the Monterey Bay in California (Lindsey *et al.* 2019) and in the North Sea (Williams *et al.* 2019). The latter study recorded 0.36 Hz Scholte waves which they associated with the secondary microseism generated by opposing ocean surface gravity waves at 0.18 Hz. Microseismic noise recorded by DAS was recently used to perform ambient noise tomography of the shallow subsurface (Spica *et al.* 2020; Cheng *et al.* 2021) and to reveal small-scale crustal structures such as an underwater sedimentary basin and faults (Lior *et al.* 2021a).

Motivated by the new capabilities of DAS, we analyse the generation of microseisms through the coastal reflection of gravity waves with highly favourable characteristics in terms of sensitivity, spatio-temporal resolution and spatial extent. Our analysis is based on a 41.5-km-long cable offshore Toulon, south of France. Using array processing techniques, we recover the azimuth, amplitude, and velocity of microseismic waves over 5 d of DAS recordings. In addition, we use the DAS measurements to quantify the ocean wave coastal reflection coefficient by computing the ratio between coastward and seaward ocean waves. We find a relatively constant coefficient of about 0.07 over the 5 d of acquisition. This new way of estimating the reflection coefficient will allow to significantly improve regional and global microseism source models.

2 DAS DATA AND PROCESSING

DAS is a photonic sensing technology that analyses Rayleigh-backscattered light in response to laser pulses injected regularly through one end of an OF cable. The light pulses are scattered by nanometric-scale heterogeneities along the OF. Axial strain in a given section of the OF, caused by external mechanical waves or by temperature variations, induces a linear phase shift of the light backscattered by that section. The phase changes arising between subsequent pulses, averaged over a given distance called the gauge length, provide a measure of strain or strain-rate at fixed locations along the fibre.

For this study, we sensed an OF cable located offshore Toulon, south of France, which was originally deployed for the MEUST-NUMerEnv project (Mediterranean Eurocentre for Underwater Sciences and Technologies—Neutrino Mer Environment, Lamare 2016). Its length of 41.5 km, and depth ranging from 0 m on the continental shelf down to 2500 m on the deep-abyssal plain (Fig. 1), enables probing both ocean surface gravity waves near the shore and seismic waves all along the cable. The cable features two near-perpendicular segments, one oriented roughly north–south and the other east–west, which we will leverage to locate the sources of microseismic noise through beamforming and back-projection. We use continuous strain-rate records which were acquired using a legacy generation-A1 DAS interrogator developed by Febus Optics, from 19 to 23 February 2019. See also Sladen *et al.* (2019), Lior *et al.* (2021b) and Rivet *et al.* (2021) for more details. With a gauge length and channel spacing of 19.2 m, the cable comprises 2100 equally spaced sensing points (channels) recording strain-rate on the seafloor. Raw continuous DAS data were recorded at a temporal sampling rate of 2 kHz, producing 16 TBytes of data. We applied a lowpass filter at 5 Hz followed by downsampling of the data by a factor 200, reducing the temporal sampling rate to 10 Hz, which is sufficient for the study of microseismic noise and gravity waves. We further reduced the volume of data by selecting 8-min-long windows every 30 min.

As an example, a 1-min-long sample of processed data is shown in Fig. 2. The cable enters the water at a distance of 1.316 km from the DAS interrogator installed at the on-land end. We begin to record ocean surface gravity waves at 1.6 km from the interrogator, where the cable exits a concrete conduit. The first kilometre of the cable after it leaves the shore is submersed at shallow depths (up to a few tens of meters) and the recordings for this section are dominated by gravity wave signals reaching a peak amplitude of several hundred nanostrain s^{-1}. Further away from the coast, the cable depth increases and the amplitude of the gravity wave signals decreases rapidly, until they are no longer visible at depths around 90 m, 5km from the shore. At depths greater than 1000 m, shorter-period waves with higher propagation velocity and lower amplitudes (a few tens of nanostrain s^{-1}) dominate the records. Their dominant frequency decreases as the depth increases reaching 0.4 Hz at 2500 m depth (Sladen *et al.* 2019). Finally, the data exhibit segments with values of strain-rate close to 0 nanostrain s^{-1} corresponding to OF segments that are weakly coupled. For instance, the 27.5–32 km segment has been replaced in 2017 and the natural burial of the cable into the soft
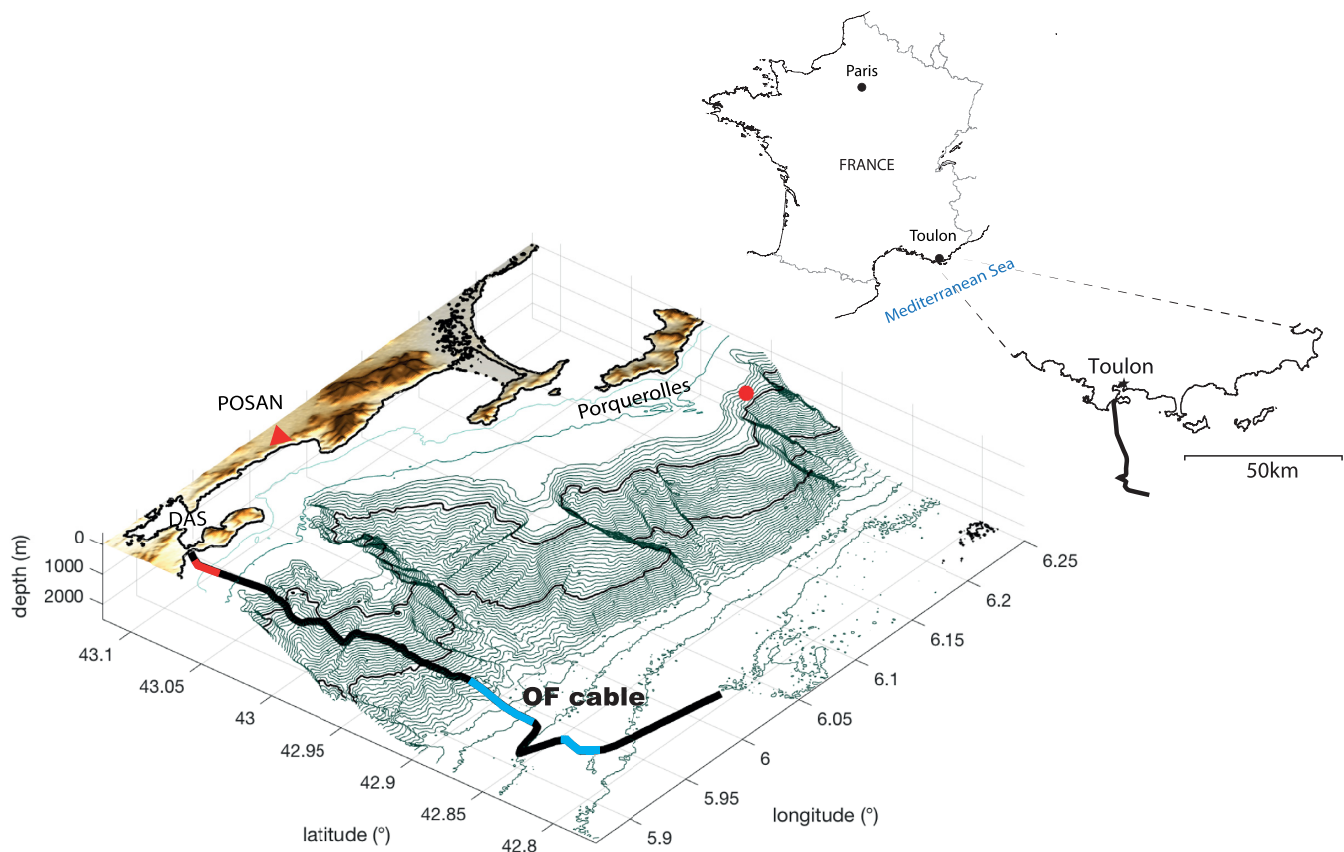
Figure 1. Map and perspective view of the seafloor MEUST- NUMerEnv cable (black curve). The red section is used to generate the *f–k* analyses in Fig. 5, and the blue sections are used in Fig. 6. The Porquerolles oceanographic buoy is indicated by the red circle. The red triangle is the permanent seismic station POSAN.

sediment is not yet sufficient to provide good coupling. Other segments are probably hanging sections (around 20 km or 34 km) that do not record Scholte waves and display cable waves (Flores *et al.* 2021; Chang & Nakata 2022). The strain-rate of these segments is set to 0. More information about this OF cable can be found in Lior *et al.* (2021b).

In addition to seafloor DAS data, we use gravity wave train data, such as wave significant height, period and direction, recorded by an oceanographic buoy (Coriolis.eu.org) located 5 km off Porquerolles island, about 20 km east from the cable (red dot in Fig. 1). We also use seismic data from the onshore permanent broad-band station POSAN (Deschamps & Beucler 2013) located close to the OF cable (red triangle in Fig. 1) to confirm the results of the DAS analysis.

3 MONITORING GRAVITY WAVES

It has been shown that surface gravity waves produced by swells and winds can be recorded by cables laid on the seafloor using DAS (Sladen *et al.* 2019; Lindsey *et al.* 2019; Williams *et al.* 2019). Strain-rates recorded along the cable induced by gravity waves are consistent with the linear wave theory (Sladen *et al.* 2019); they are proportional to wave height and depend on the ratio of water depth to wavelength. The geometry of the cable used in this study enables us to identify the characteristics of gravity waves at different depths and to make precise measurements of oceanic waves over the 5-d time-series. For the shallowest section of the cable (between 10 and 80 m depth), we computed the absolute value of the strain-rate, and plotted the mean value over each 8-min-long window

(Fig. 3a). Most of the ocean gravity wave energy is located in the 10–45 m depth range. As observed by Sladen *et al.* (2019), the energy decays rapidly with depth (below about 20 m depth) which is consistent with the linear gravity wave theory. The significant wave height simultaneously recorded at the Porquerolles buoy and the amplitude of strain-rate recorded along the cable at different water depths are plotted in Fig. 3(b). The values of both quantities decrease from the beginning of the time-series, then rise to a first peak before 21 February barely visible at shallow depths. This small peak is followed by the biggest peak on 21 February clearly visible on DAS data at all depths sensitive to gravity waves. A divergence emerges after 22 February, especially at the larger depths where a slower decrease in strain rate is observed. This demonstrates that the strain-rate amplitudes are related to local weather conditions changes captured on the buoy data. Note that we are comparing first-order data from a buoy located 25 km away from the cable, above a 900 m water column, to strains recorded on the OF cable at shallow depth (less than 50 m). Although we focus here on the similarities, we do not overlook the fact that there are differences between these two data sets.

A good correlation is also found between the dominant frequency of strain-rate recorded at, for example 30 m depth and the ocean wave frequency recorded by the buoy (Fig. 4b). The most energetic spectral components of the strain-rate are consistent with the ocean wave frequency range (from 0.1 to 0.3 Hz) recorded at the sea surface by the buoy (red curve). There is also a similarity between the time-series of significant wave height and the peak spectral amplitude at the selected 30-m-deep DAS sensor (grey and red
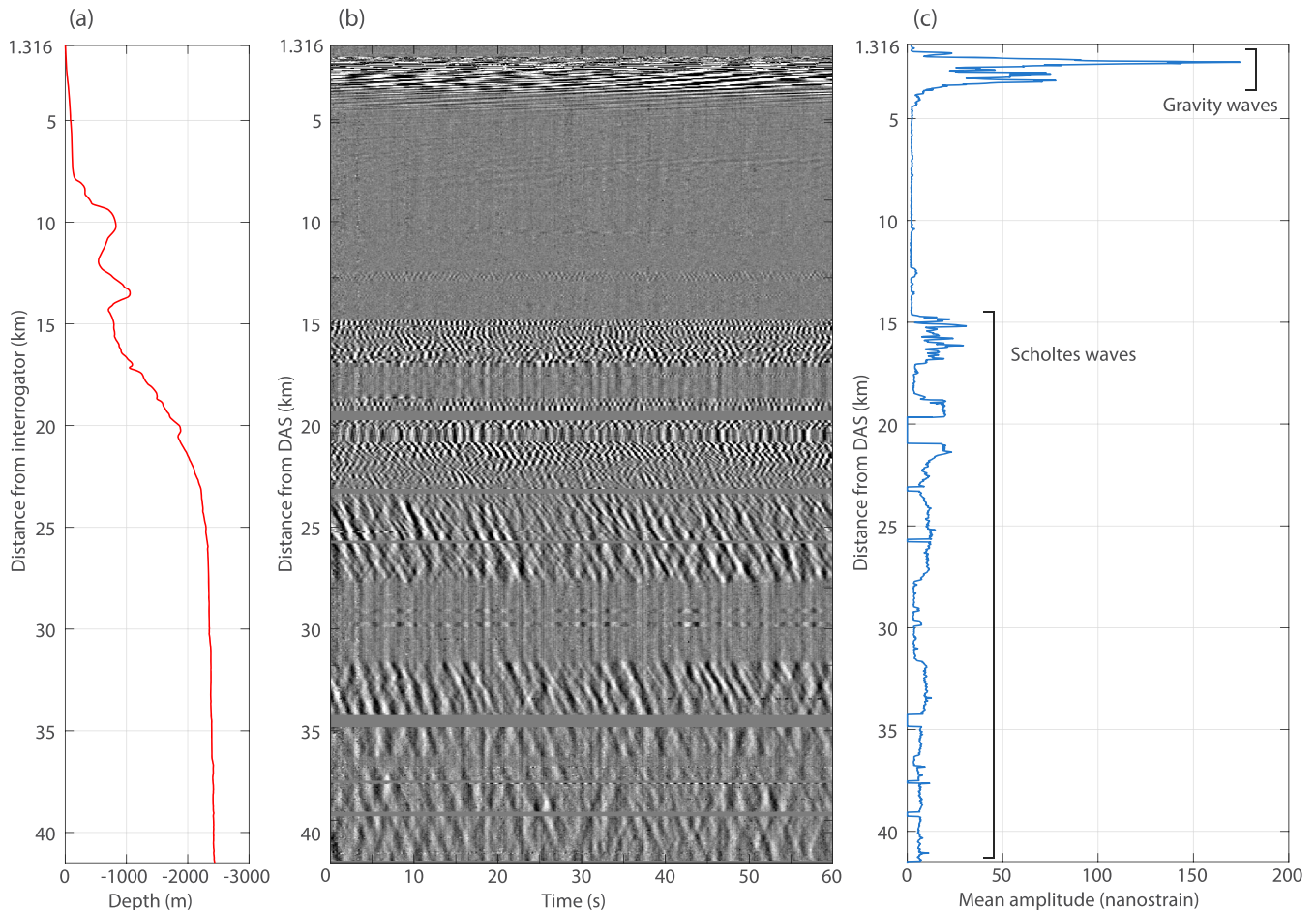
Figure 2. Data sample. (a) Depth profile of the OF cable. (b) 1-min-long record of strain-rate at distances of 1.3–41.5 km along the cable relative to the DAS interrogator. (c) Mean absolute strain-rate along the fibre. Note that the amplitudes of the gravity waves are very large compared to the microseisms.

curves, respectively, in Fig. 4a). This confirms that we can use DAS to monitor the amplitude and spectral content of the ocean surface gravity waves that propagate above the OF cable.

The high spatial coherence of the gravity waves measured up to 5 km distance permits a characterization of the gravity wave propagation direction, but it is not possible with the linear array geometry to accurately determine the ocean wave directional spectrum from the *f–k* analysis without knowing its velocity. In addition, the DAS data enables an estimation of the fraction of the waves that are reflected at the coast. Fig. 5(a) shows the frequency–wavenumber (*f–k*) decomposition of the strain-rate signals on a linear cable segment near the shore (from 2 to 5 km), over four time windows that capture various ocean wave conditions characterized by distinct values of the normalized significant wave height (Fig. 5b). We compare the observed dispersion curves to the theoretical dispersion curve of the linear gravity wave theory (Lamb 1945):

$$\omega = \sqrt{gk \tanh(kh)}, \tag{1}$$

where g is the acceleration of gravity, ω the temporal frequency, k the spatial wavenumber and h the water depth. We set the latter to 50 m, the average depth of the selected cable segment; considering that its depth ranges from 15 to 100 m, this assumption may produce small discrepancies on the theoretical dispersion curves. Note that gravity waves propagating in different directions, corresponding to different apparent speeds along the cable, should appear in the *f–k* diagram as separate streaks. In fact, the wavenumber variable of our

f–k plots is the apparent wavenumber $k_{app} = k\cos(\theta)$, the projection of the wavevector onto the cable direction, where θ is the wave propagation angle relative to the cable orientation. Fig. 5 shows the theoretical dispersion curves as a function of k_{app} for two angles of incidence, $\theta = 0°$ and $60°$, computed with eq. (1) after setting $k = k_{app}/\cos(\theta)$.

Most of the energy recorded at the depths selected in Fig. 5 propagates landward and has frequencies between 0.05 and 0.20 Hz. In the *f–k* diagrams, dispersive group velocities are given by the local tangent $\partial\omega/\partial k$. They range from 10 to 25 m s^{-1} and depend on wavelength. When the swell height is at its highest (time stamp 3), the energy is more spread out in *f–k* space and has a peak at azimuth 60° located at lower wavenumbers, corresponding to higher velocities. We further investigate the azimuth and velocity of the gravity waves by beamforming analysis in Section 6.

As shown on the *f–k* analysis of ocean surface gravity waves, a significant part of the energy is reflected (Elgar *et al.* 1994), and can be quantified thanks to the dense network of sensors provided by DAS. The top panels of Fig. 5(a) show the normalized energy as a function of wavenumber at time stamps 1 to 4. We integrated across frequencies between 0 and 0.2 Hz that correspond to the range of gravity wave frequencies. At all times, the energy exhibits a bimodal distribution with two local maxima corresponding to the landward (right) and seaward (left) propagation of the gravity waves. Regardless of the strength of the swell, a significant amount of gravity waves amplitude (from 20 to 30 per cent) is reflected at the coast.
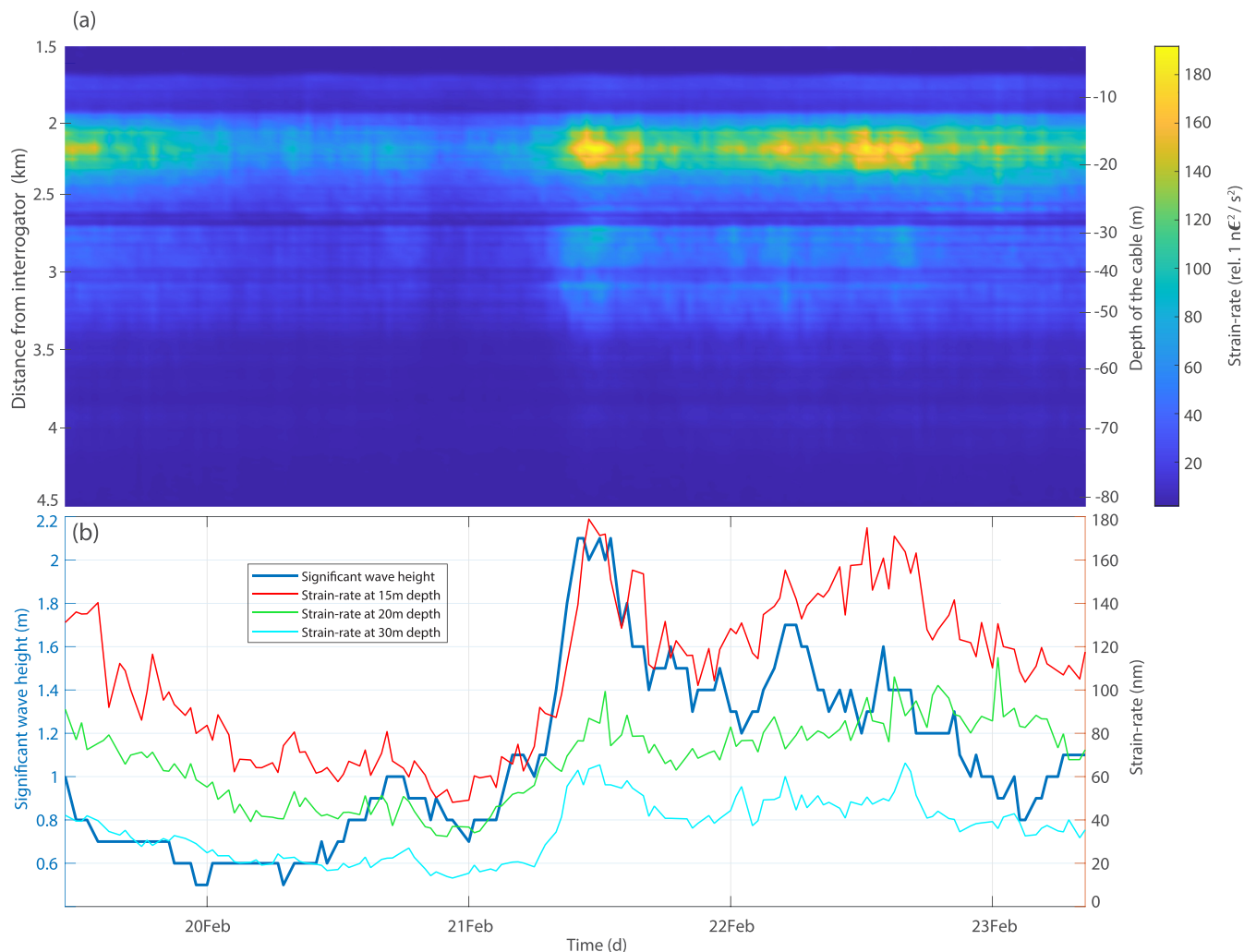
(a)

(b)

Figure 3. Observations of surface gravity waves. (a) Amplitude of strain-rate recorded between 1.5 and 4.5 km from the interrogator over 5 d. Warm colours represent the maximum mean amplitude. The right vertical axis is the depth of the cable. (b) Significant wave height recorded at the buoy off Porquerolles Island over 5 d (blue) and the DAS strain-rate measured at different depths: 15 (red), 20 (green) and 30 m (cyan).

We computed the mean energy of the seaward ($k < 0$) and coastward ($k > 0$) propagating waves at frequencies ranging between –0.3 and 0.3 Hz for both components and wavenumbers ranging between 0 and ±0.03 m^{-1} (Fig. 5b). As expected, the energy in the coastward direction is correlated with the relative water level recorded at the buoy (blue curve), which controls the significant waves height. The reflected waves (seaward) follow a similar evolution, at least when the swell is at its highest (time stamp 3).

We compute the reflection coefficient R^2 defined as the ratio of seaward to coastward wave energy (Elgar et al. 1994). When the swell is not strong enough, the energy of the reflected gravity waves is too low to reliably estimate the reflection coefficient. We disregard the reflection coefficient computed when the seaward energy is below a threshold of about 52 dB (horizontal red line), defined as the average energy during 5 d on a segment of the cable where we do not record gravity waves (around 7 km from the interrogator). When the swell is low, the seaward wave energy falls below the threshold, resulting in inflated R^2 values of up to 0.14 (light grey rectangles in Fig. 5c). In periods with seaward energy above the threshold, the reflection coefficient is rather stable around the average value $R^2 \approx 0.07$ in the 0.05–0.20 Hz frequency range, which corresponds to 26 per cent relative amplitude between reflected and incident

waves. For comparison, Elgar et al. (1994) found a value of $R^2 \approx$ 0.05 in the 0.1–0.15 Hz frequency range on a plane sloping beach similar to our experiment (which has a slope of around 2 per cent), and Stutzmann et al. (2012) estimated an average $R^2 = 0.02$ for the French continental seismic station SSB of the GEOSCOPE network.

R^2 may vary with wave frequency. Fortunately, during the 5-d experiment, the gravity wave period evolved, and so we are able to investigate its properties by estimating the R^2 at different frequencies (Fig. 6a). For a given frequency, R^2 is constant regardless of the energy of the swell. When the swell is low, between 20 and 21 February, the results are biased by the high noise level. When the swell is at its maximum (shown as a function of frequency in Fig. 6b), the mean R^2 increases with frequency, from 0.08 at 0.1 Hz to 0.14 at 0.2 Hz. At higher frequencies, the amplitude of the ocean surface gravity waves is too low to calculate R^2 reliably.

Overall, we estimate that at least 25 per cent of the gravity waves amplitude are reflected. The interference between landward and reflected seaward waves is expected to generate secondary microseisms in the coastal region. In order to quantify this mechanism and its contribution to the overall ambient noise wavefield, we next investigate the Scholte waves recorded at further depths, between 1000 and 2400 m.
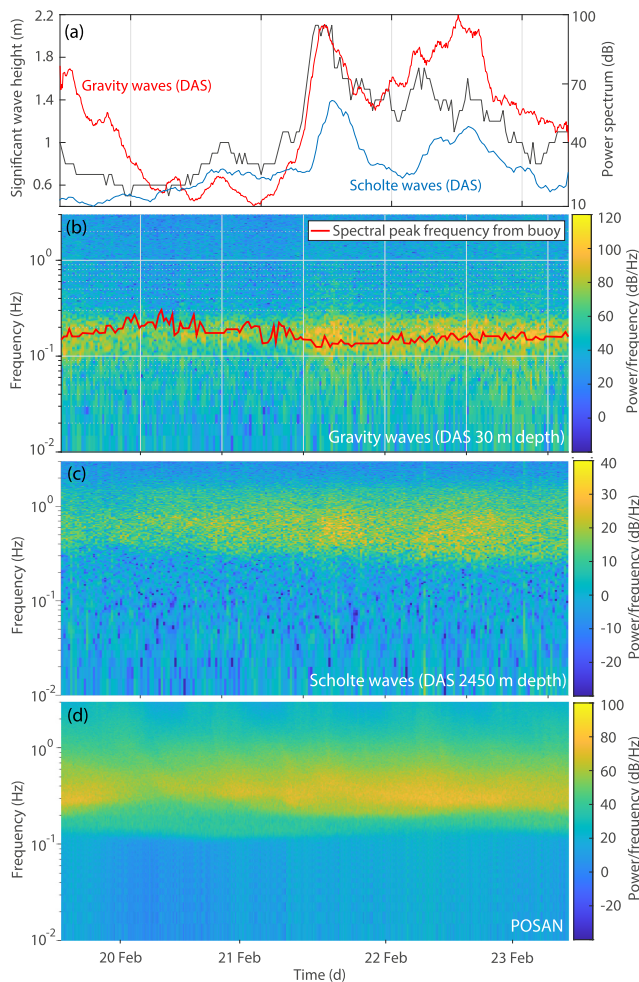
Figure 4. (a) Time-series of significant wave height recorded by the Porquerolles buoy (grey), strain-rate power at 30 m depth dominated by gravity waves (red), and strain-rate power at 2450 m depth dominated by Scholte waves (blue). The strain rate axis is on the right. Spectrograms over 5 d, from Febraury 19 to 23, of (b) strain-rate at 30 m depth, (c) strain-rate at 2450 m depth and (d) ground motion recorded by an onshore broad-band station (POSAN) located near the DAS interrogator. The red curve in (b) is the spectral peak frequency of ocean wave height recorded at the buoy.

4 SECONDARY MICROSEISMIC SCHOLTE WAVES

Farther along the fibre, from the continental slope (1500 m depth) to the abyssal plain (2500 m depth), DAS recordings are dominated by higher velocity, dispersive, continuous wave trains with frequencies ranging from 0.25 to 1.3 Hz (Fig. 7). Sladen *et al.* (2019) showed that these wave trains are Scholte waves propagating at the fluid–solid interface in both coastward and oceanward directions. These seismic waves are generated by the interaction of gravity waves with same frequency and wavenumber but opposite directions, which is known to cause second-order pressure variations that constitute secondary microseism sources (Longuet-Higgins 1950; Hasselmann 1963). The wide range of frequencies from 0.25 to 1.5 Hz (which exceeds twice the frequency of gravity waves) seen on the *f*–*k* analysis and on the spectrogram (Fig. 4c) is due to resonance in the water layer that amplifies certain frequencies depending on the height of the water column (Sladen *et al.* 2019). This effect almost vanishes in

the abyssal plain at 2500 m depth, where the frequencies range from 0.25 to 0.4 Hz.

The amplitude of the Scholte waves between 0.25 and 0.7 Hz follows the fluctuations of the significant wave height recorded at the buoy (Fig. 7a), even if time-shifts of a few hours appear (notably on 21 and 22 February). Similarly, these patterns of increase and decrease can be seen on the spectrogram of strain-rate at a deep location in the abyssal plain (Fig. 4c). When the swell increases on February 21, the strain-rate power does too. The spectrogram of the onshore broad-band station POSAN (Fig. 4d) shows a similar frequency range as that of the abyssal plain DAS data, between 0.25 and 0.5 Hz, and its amplitude fluctuations are correlated with the significant wave height recorded by the buoy some 50 km away. The temporal correlation between the swell amplitude and Scholte wave amplitudes suggests that a large proportion of the secondary microseism recorded on the OF cable is caused by local weather conditions and is generated by the local interaction of incident and coastal-reflected ocean waves. The same applies for the inland station POSAN. However, a significant amount of energy coming from offshore sources located at further distance (non-local) is recorded on the OF cable and contributes to the general level of microseismic noise in the area.

5 DELAY BETWEEN BUOY SIGNIFICANT WAVE HEIGHT AND DAS SEAFLOOR STRAIN

In order to better understand the delay between the relative wave height and the Scholte wave power (Fig. 7a), we will compare the lags between the coastward component of ocean surface gravity waves (Fig. 8) and the oceanward component of Scholte waves (Fig. 9) with the significant wave height measured at the buoy. We choose these components, the most energetic for each wave type, because they seem to be related through coastal reflection to the local sea conditions that are more relevant for this work. We first compare the times-series of the mean coastward energy measured on the shallow section of the cable (i.e. the ocean surface gravity waves) and the amplitude of the significant wave height measured at the buoy (Fig. 8a). The two quantities seem to follow the same dynamics of increasing and decreasing amplitude. However, a short delay is observed, especially in two periods indicated by the black rectangles on Fig. 8(a). At the peak of the swell, in the period labelled 1, the DAS strain is delayed by about 45 min relative to the significant wave height. In the period labelled 2, the time-shift is of similar amplitude but of opposite sign. These time-shifts are consistent with the propagation direction of the swell, quantified at the buoy by the wave direction at the frequency of the peak (blue curve in Fig. 8b). The variability in wave direction (called spreading) is low (10°) for label 1, and shows values ranging from 70° to 90° for label 2 (not shown on figures). In the period labelled 1, the swell backazimuth is 100° (it comes from the east), thus it first arrives at the buoy and then at the fibre. Likewise, in the period labelled 2, the wave direction changes from a steady value to a volatile value of about 250°. That means that the ocean waves will be recorded first on the cable, then on the buoy, which is consistent with our results.

Similar to the analysis we performed on the gravity waves, we computed the oceanward component from the *f*–*k* decomposition for the 21–35 km north–south linear segment over the full time-series (red curve on Fig. 9) to compare it to the significant swell height (blue curve). Before February 21, when the swell is low, the two quantities have discrepancies, although the increase that starts
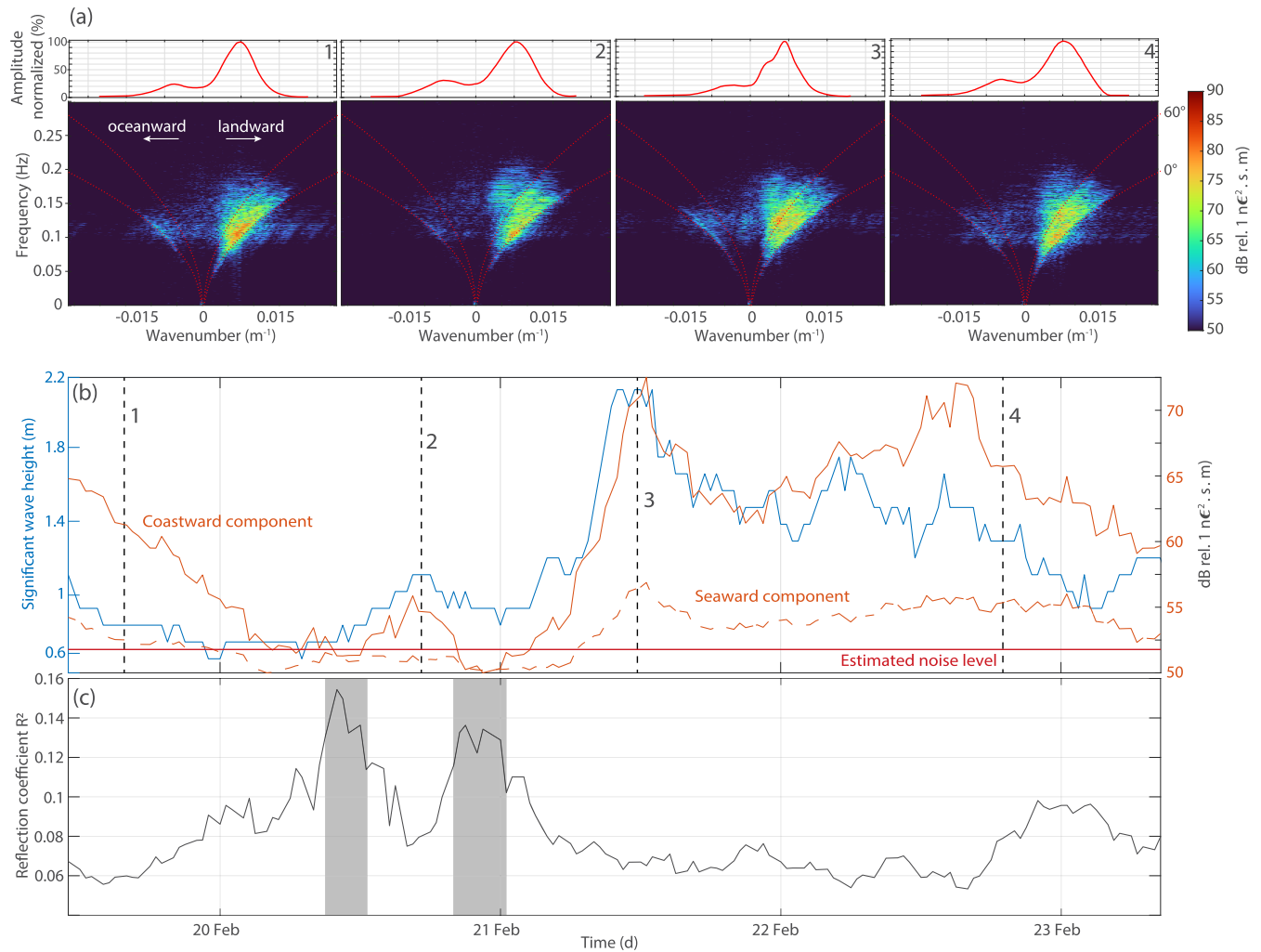
Figure 5. (a) Top panel: strain-rate amplitude between 0 and 0.3 Hz as a function of wavenumber, normalized by the maximal power, and bottom panel: frequency–wavenumber (*f*–*k*) decomposition of the strain-rate signal for seaward and landward components, along a cable segment between 2 and 5 km indicated in Fig. 2(a), at four different times indicated in (b). Red dotted curves are the theoretical dispersion curves of gravity waves for two different incidence angles, 0° and 60° relative to the cable orientation. (b) Significant wave height recorded at the buoy off Porquerolles Island over 5 d (blue curve), seaward and coastward energies (solid and dashed red curves, respectively) and estimated noise (horizontal red line). The vertical black dashed lines with numbers indicate selected times with different ocean wave conditions for *f*–*k* analysis. (c) R^2 reflection coefficient, defined as the ratio of seaward to coastward energy, computed from a *f*–*k* decomposition over 5 d, by stacking the *f*–*k* decomposition of 8-min-long strain-rate windows every 30 min.

in the middle of February 21 can be seen on both curves. After the February 21, the tendency of *f*–*k* decomposition energy is correlated with the swell but with some time delay.

If we focus on the peak of the swell (rectangle label 1), we can see a large shift of around 90 min when the swell get stronger while the shift is much smaller (about 30 min) when the swell weakens. Later, on rectangle labelled 2, the oceanward component (red curve) seems to increase before that the swell goes up. Looking at the direction of the swell (Fig. 8b), we can see that it changes from 100° (southeast direction) to 250° (southwest direction).

6 BEAMFORMING MICROSEISM SOURCES

At this point, we have followed several lines of evidence indicating that most of the coherent noise recorded as Scholte waves on the OF cable was correlated to the local weather. Therefore, we hypothesize that secondary microseism sources are located near the coast. We

now aim to better characterize the direction-of-arrival (azimuth) and apparent velocity of the coherent waves through beamforming analysis for each cable segment that exhibits sufficient signal to noise ratios. A common assumption in seismic beamforming is that the recordings of a seismic array result from a superposition of plane waves carrying a specific signal, striking the array at a given angle of incidence. The relative time delays across the array are computed for each candidate slowness and backazimuth pair over a grid of values, then translated into vectors of phase shifts known as the steering vectors. The beampower for each combination of slowness and azimuth is computed by projecting the steering vectors onto the covariance matrix C_{ij}, defined as:

$$C_{ij} = \frac{1}{N} \sum_{n=1}^{N} \left[Y_i(n) Y_j^{\dagger}(n) \right] \quad (2)$$

in which Y is the Fourier-transformed strain-rate data measured at a given sensor, n is the frequency index within a specified frequency band of size N, and † denotes complex conjugation. For this study, we
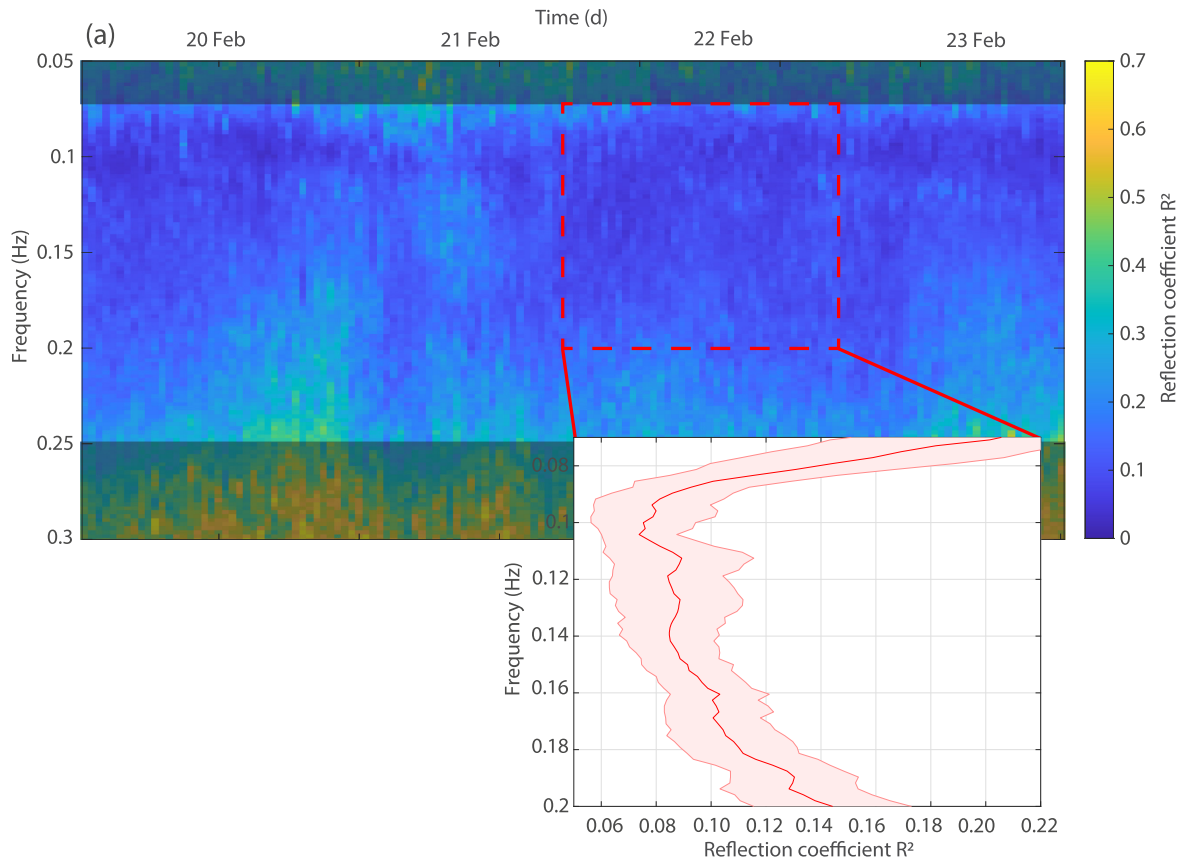
Figure 6. (a) Reflection coefficient R^2 computed for each frequency between 0.05 and 0.3 Hz. (b) Mean reflection coefficient R^2 for frequencies ranging from 0.075 to 0.2 Hz at the highest swell. Lighter red band shows the standard deviation.
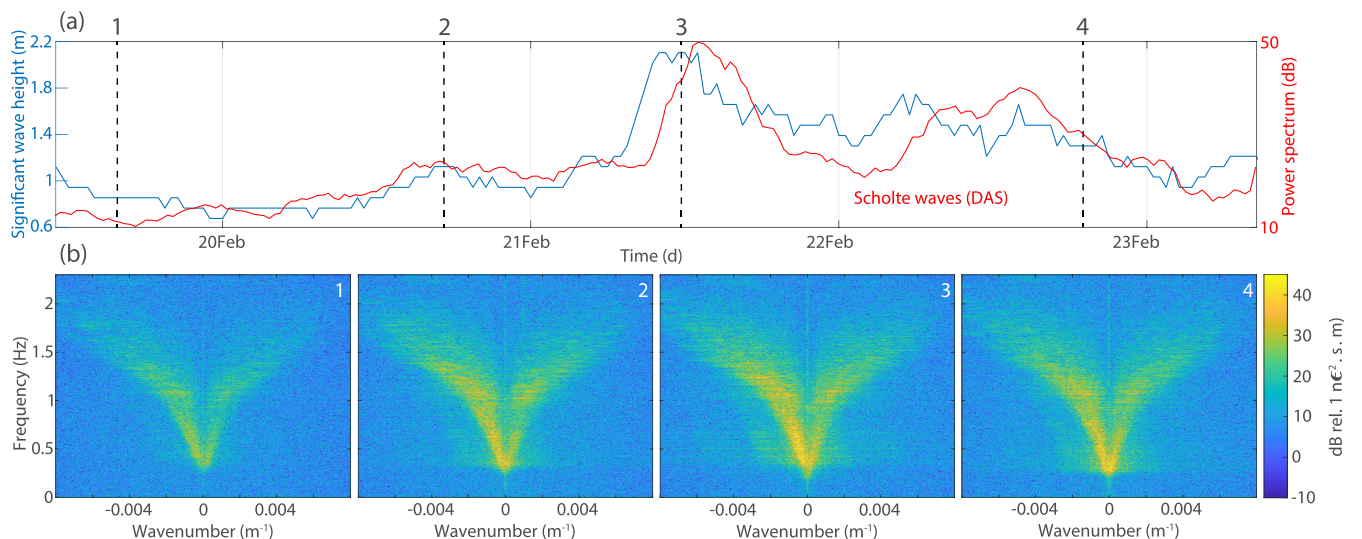

Figure 7. Observations of oceanic secondary microseismic noise. (a) Normalized significant wave height (in m) of the local swell recorded at the buoy off Porquerolles Island over 5 d (blue curve). The red curve shows the strain-rate power between 0.25 and 0.7 Hz recorded by DAS at 2450 m depth, which is dominated by Scholte waves (plotted also on Fig. 4). (b) Frequency–wavenumber (*f–k*) decomposition of the strain-rate signal of the 21–35 km north–south segment, for seaward and landward components.

use an extension of classical beamforming analysis called MUltiple SIgnal Classification (MUSIC, Schmidt 1986). MUSIC achieves higher-resolution direction-of-arrival estimates by minimizing the projection of the steering vectors onto the noise-space of C_{ij}, defined by its M smallest eigenvectors. For details of the method we refer to Schmidt (1986), Goldstein & Archuleta (1987) and Meng *et al.* (2011). van den Ende & Ampuero (2021) demonstrated the potential of MUSIC beamforming analysis applied to DAS arrays by analysing an M_L 4.3 earthquake. Since beamforming on a linear array only reveals the *apparent* propagation velocity (the projection
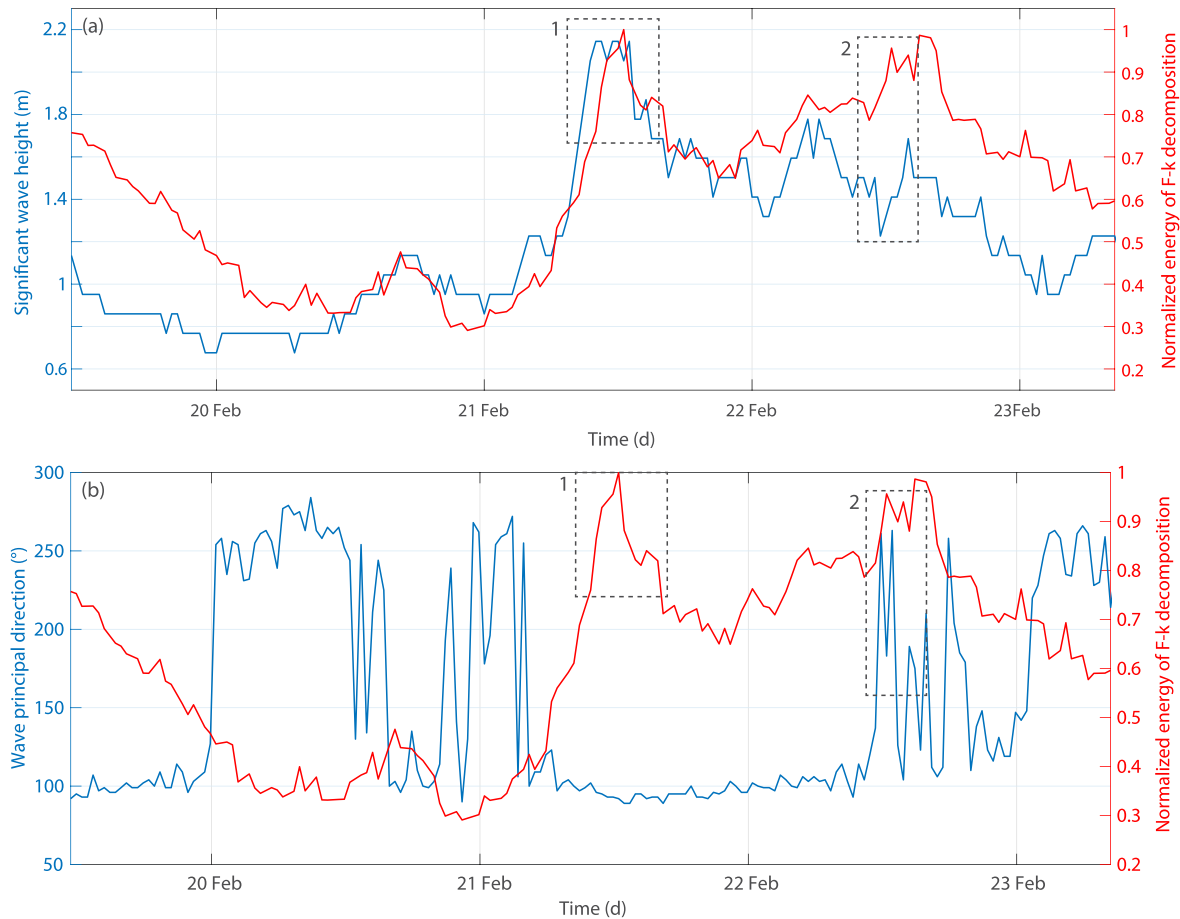
Figure 8. Mean of the seafloor strain-rate amplitude of ocean surface gravity waves travelling coastward estimated on the *f–k* decomposition over the 5 d of DAS data (red curve), plotted together with (a) the significant wave height (*m*) recorded at the buoy (blue) and (b) wave principal direction (degree) recorded at the buoy (blue). Black dotted rectangles highlight periods with visible time-shifts between the two time-series shown in (a).
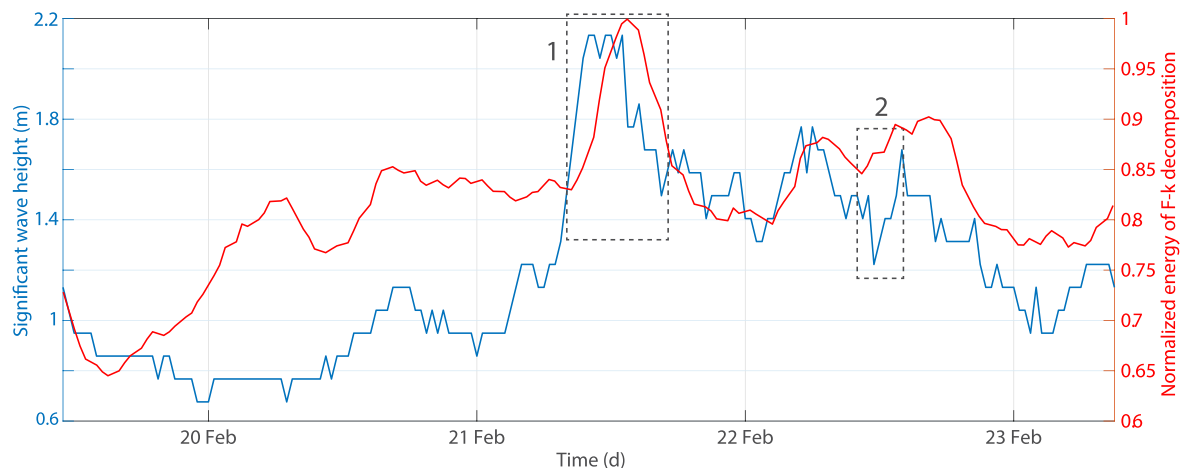

Figure 9. Mean of the oceanward components of the *f–k* decomposition of Scholte waves over the 5 d of data (red) and significant wave height (m) recorded at the buoy (blue). Black dotted rectangles highlight delay.

of wave velocity onto the array orientation), a trade-off between the apparent velocity and backazimuth emerges for linear arrays. For the analysis of gravity waves, only one linear segment of the cable is available, which will inevitably suffer from this geometrically induced ambiguity. However, for the beamforming of the Scholte waves, this ambiguity is resolved by using two quasi-perpendicular

segments of the cable: a 17.5 km long south–north segment and a 9 km long west–east segment containing multiple linear portions.

To set a baseline, we first beamform the shallow-depth gravity waves recorded at specific times by using a linear segment used previously for the *f–k* decomposition (Fig. 1). Pre-processing consists
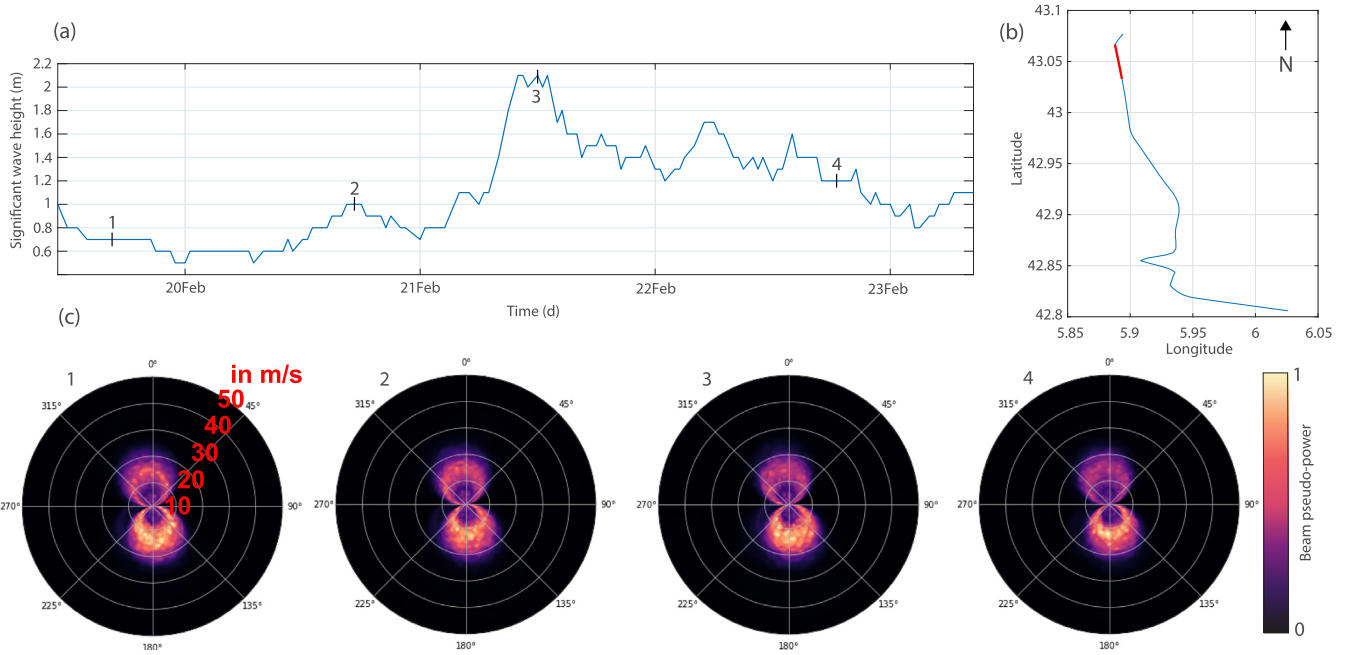
Figure 10. (a) Significant wave height (in m) of the local swell recorded at the buoy off Porquerolles Island over 5 d. (b) Location of the cable segment (red curve) along the cable. (c) Beamforming results in the 0.2–1.5 Hz frequency band for different times indicated by the numbers above each panel and on the time-series in (a).
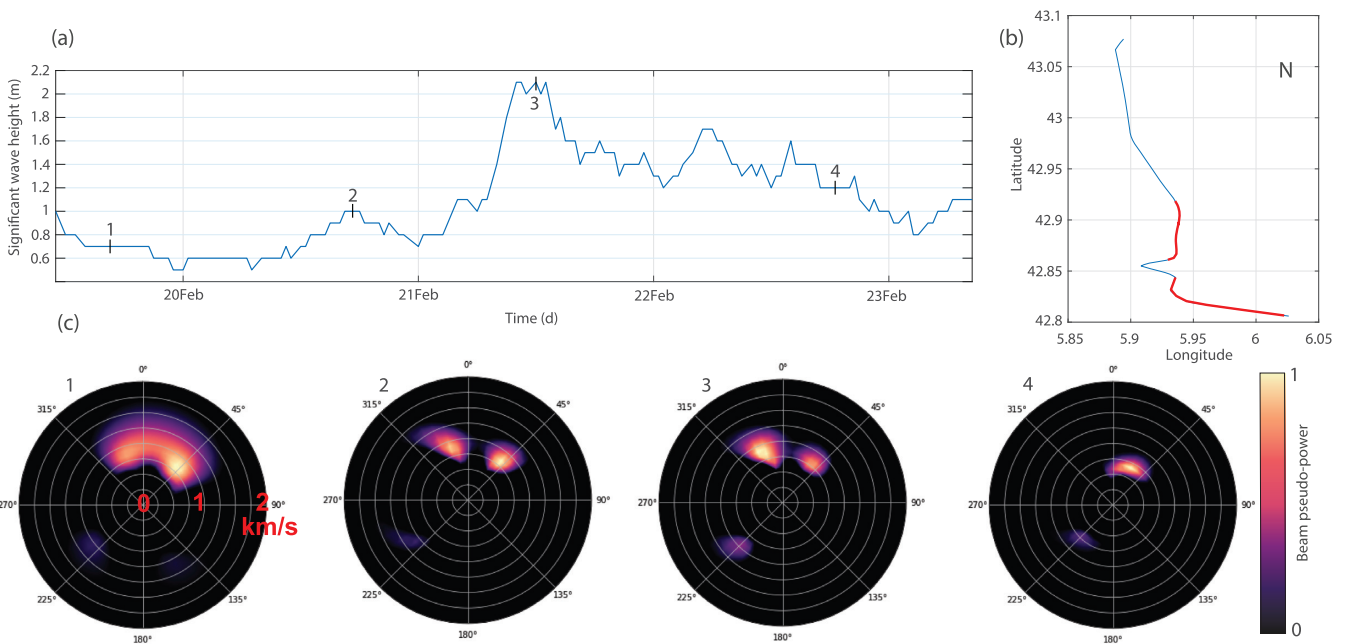

Figure 11. (a) Significant wave height (in m) of the local swell recorded at the buoy off Porquerolles Island over 5 d. (b) Location of the segment (red curve) along the cable. (c) Beamforming results in the 0.25–1 Hz frequency band for different times as indicated by the numbers above each panel.

of applying a taper and bandpass filter from 0.05 to 0.2 Hz. Then, each trace of the signal is normalized by its standard deviation. Due to the trade-off between velocity and azimuth on linear arrays discussed earlier, beamforming results in a ring pattern for each incident wave in velocity-azimuth polar plots (Fig. 10c). As expected, assuming a finite apparent velocity, the south backazimuth ring (i.e. swell coming from the sea) exhibits a stronger coherence than the northern one, with apparent velocities between 15 and 30 m s^{-1} (Fig. 10c). These results are consistent with the nature of the ocean

surface gravity waves recorded on the OF cable. Additionally, there are no significant differences between the four selected time periods. Since this shallow part of the cable constitutes a linear array, we are unable to precisely pin-point the backazimuth.

Motivated by the consistent results obtained in the gravity wave beamforming, we now turn to locating the source of Scholte waves recorded along the OF cable. To break the ambiguity in the backazimuth and apparent velocity, we consider all segments with sufficient coupling in the beamforming procedure. We tested two methods to
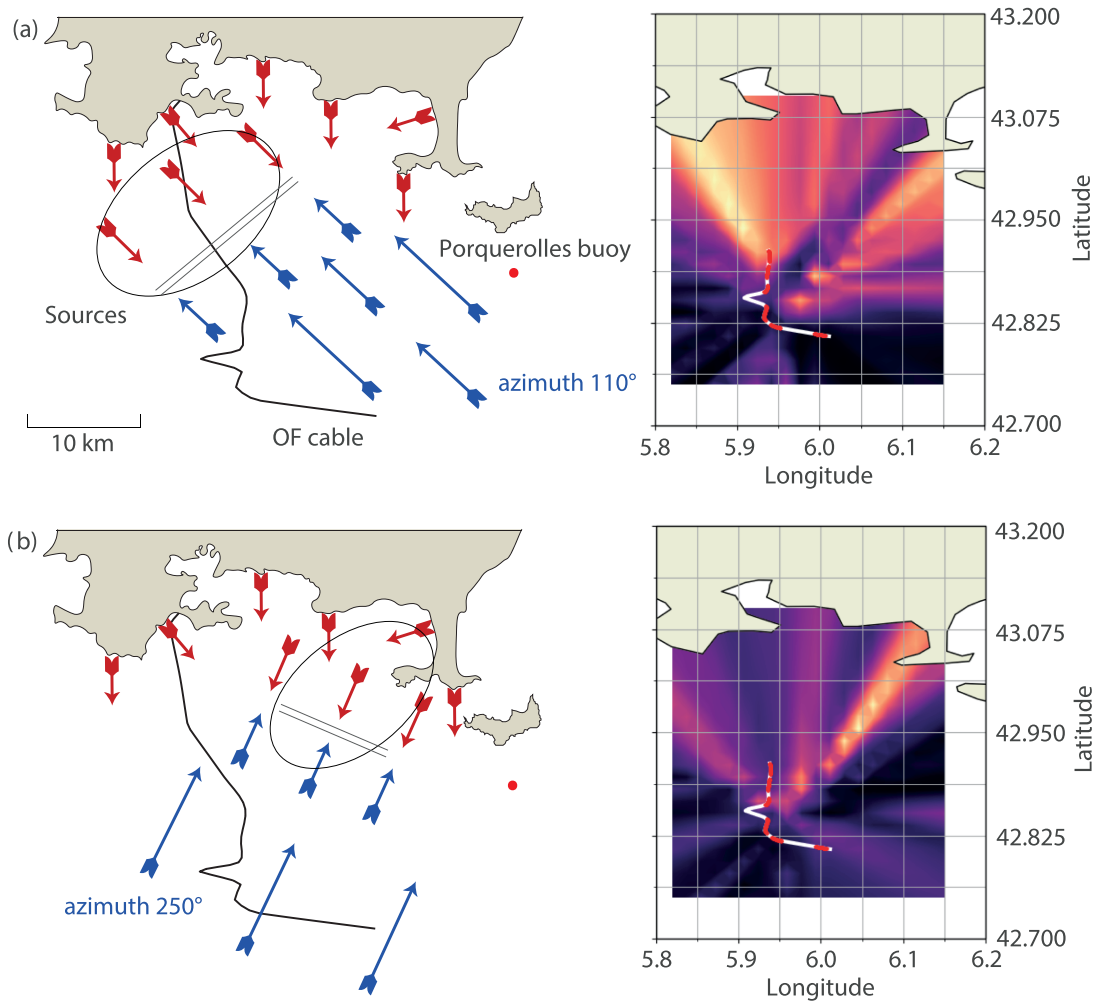
Figure 12. Conceptual model of the coastal reflection sources with the associated back-projection on the right side. The blue arrows are the incident ocean surface gravity waves and the red ones are the reflected gravity waves. The double grey lines correspond to the location of the secondary microseismic source computed using the delays. The ellipses correspond to the sources computed using the backprojection analysis. The warm colours in the figures on the right indicate the location of the sources. (a) The gravity waves come from a southeast azimuth (Fig. 9—label 1). (b) The gravity waves come from a southwestern azimuth (Fig. 9—label 2).

combine the different segments. The first method is to beamform each segment separately and combine them with a harmonic mean while the second method applies beamforming to all the segments together. The resulting beams are slightly better resolved with the first method. Furthermore, in order to better see the waves coming from the open sea, we apply a *f–k* filtering and isolated the negative and positive parts which correspond, respectively, to the waves coming from the coast and the waves coming from the open sea. Then we calculate separately the beam power of these two quantities and combine them through a harmonic mean.

As shown in Fig. 7(b), the secondary microseismic noise is recorded on a wide frequency band, so we bandpass filter each 120-s-long time period between 0.25 and 1 Hz. The selected segments are aligned along two dominant azimuths (0° and 100°, respectively) with a nearly similar length so that the contribution of each segment is fairly equal (Fig. 11b). The beamforming results exhibit well-resolved sources pointing in the north direction with an apparent velocity of 1 km s^{-1} which are consistent with Scholte waves velocity. At times 1, 2 and 4, we obtain a maximum beam power at an azimuth of 45°, while we get a maximum at an azimuth of 330° for time 3. The two peaks are visible simultaneously in times 1, 2

and 3. In addition, we retrieve a lower waveform coherence coming from south azimuth (at around 225°) which indicates a source located offshore in the Mediterranean. The beamforming analysis confirmed the results of the *f–k* representations for both gravity and Scholte waves. A significant part of the gravity waves is reflected at the coast and most of the microseismic waves seems to come from the coast. The pseudo-power coming from the southwest will be discuss in the next section.

7 DISCUSSION

The high density of the seismic network provided by DAS allows us to obtain accurate and continuous information on gravity waves and microseismic noise around the OF cable. In order to record coherent signals, especially for ambient noise Scholte waves, the cable must be well coupled to the seafloor (Fig. 2b). The strain-rate induced on the OF cable by the ocean surface gravity waves can be monitored over the time-series and used to recover both the relative amplitude and frequency of ocean waves. By performing beamforming analysis on DAS data, it is possible to obtain well resolved sources (Fig. 10), but with an ambiguous apparent

velocity and azimuth since the segments used are linear. These results demonstrate that under certain circumstances (geometry of the array, good coupling), sea state monitoring is possible leveraging DAS. We showed that DAS recordings are dominated by gravity waves, with speeds from 15 to 30 m s^{-1}, near the coast (from 10 to 60 m depth), and their amplitude decays rapidly with depth. Deeper (around 900 m depth), gravity waves are no longer recorded and the continuous DAS records are dominated by the faster Scholte waves, with speeds around 1000 m s^{-1}, but with lower amplitudes (Fig. 2c). The temporal evolution of the power of both the gravity and Scholte waves (Fig. 4a) are in agreement with that of the amplitude of the swell recorded at the buoy, suggesting that a large fraction of the microseismic noise recorded by the DAS is generated by local coastal sources resulting from the interaction of incident and coast-reflected ocean waves. Therefore, continuously recorded signals (0.1–1.5 Hz) along the cable depend on local oceanic waves. The addition of a marine buoy closer to the cable can be an asset to confirm that the strains recorded on DAS are indeed related to the swell (Fig. 3b) and to quantitatively assess the sensitivity of the DAS to sea conditions.

Stutzmann *et al.* (2012) have shown that microseism sources generated by coastal reflection cannot be neglected on a large scale, while in this study we quantify the importance of such sources at smaller scales. In the part of the northern coast of the Mediterranean sea studied here, incident ocean waves travel from south to north. Secondary microseismic noise recorded by the DAS are dominated by coastal reflection sources close to the shore, although an unquantified but smaller portion comes from offshore (Fig. 10c). This latter distant source is also visible on a broad-band station several kilometres north onshore (Fig. 4d). To better understand whether this source from the southwest is real or an artefact, we analysed the numerical ocean wave model provided by IFREMER (Ardhuin *et al.* 2011) that gives microseismic sources all over the Mediterranean Sea with a time step of 3 hr. During the period of our data, the model shows a source near the Balearic Islands (Fig. S1), 400 km to the southwest of the OF cable, at frequencies around 0.25 Hz. The predicted source is stronger between 21 and 22 February, and is consistent with the pseudo-power amplitude obtained by beamforming analysis (Fig. 11c).

DAS measurements provide a unique way to follow the whole process that leads to the formation of coastal reflection sources: the propagation of gravity waves to the coast, their reflection at the coast and their role in the generation of microseismic sources. We estimated the reflection coefficient R^2 on a 3-km-long portion at 70 m depth (progressive slope of 2 per cent) where the recording of gravity waves is optimal (Fig. 3a). In addition, the sensitivity to gravity waves is maximized in this selected segment because the azimuth of the incident and reflected waves tends to be perpendicular to the coast, and therefore parallel to the OF when the depth is shallow (Snell's law). Between 25 and 30 per cent of these gravity waves with frequencies ranging from 0.05 to 0.2 Hz are reflected, which makes the reflection coefficient R^2 slightly lower than 0.1 on average. Ardhuin *et al.* (2012) modelled comparable values in the Hawaiian islands, which exhibit a similar shoreline. Additionally, we observe that the R^2 varies with values between 0.06 and 0.1, when the significant wave height is high enough to produce reflected waves that are detected above the noise floor (Fig. 5c). In this case, we see that the R^2 increases slightly as the significant wave height decreases and vice versa. To further investigate, we calculated the reflection coefficient for each frequency, which shows that the R^2 remains nearly constant over the 5 d of experiment for a given frequency, but varies as the frequency increases (Fig. 6a). This is in

agreement with Ardhuin *et al.* (2012), who showed that the reflection coefficient is strongly influenced by the shoreface slope and the frequency of the gravity waves travelling to this slope. Apart from that, our quantification of this dependence is limited by the too small strains induced by the ocean surface gravity waves when the swell is low. Indeed, the DAS data actually constrains the ratio between the energy of the incident wave and that of the reflected waves plus noise. As a result, the double peak increase of R^2 between 20 and 21 February is an artefact.

We measured time delays between the swell height recorded at the buoy and the amplitude of the gravity wave signal recorded on the OF cable. Similarly, delays appear on microseismic noise recordings with respect to the swell height. This is due to the distance between the buoy, the cable and the coast where gravity waves are reflected toward the backazimuth of the gravity waves. To generate secondary microseismic, one needs two wavefields with opposite direction but equal frequency. When the swell suddenly increases, the wavelength and frequency of the gravity waves change. Then, this new wavefield travels to the coast, is reflected and interacts with some delay with incoming gravity waves that have same wavenumber and frequency but opposite azimuth to generate a new secondary microseismic source. Therefore the local source of the secondary microseismic noise may move, depending on a change in the azimuth of the incident ocean waves. That particular behaviour of coastal reflections sources has been studied by Ardhuin *et al.* (2012). They showed that seismic waves amplitude have a delay of 2 hr with respect to the significant wave height measured at a buoy at a distance of 70 km.

We investigated this mechanism of secondary source generation near the coast by means of back-projection, which allows us to determine the location of the sources. We use the same framework as beamforming, but we compute the arrival times directly based on the distance and an assumed velocity model [Scholte waves at 1000 m s^{-1} taken from a *P*-wave seismic velocity model computed by Sladen *et al.* (2019)] computed over a grid of potential source locations.

This back-projection analysis paints a consistent picture with our previous analysis, namely that when the swell changes azimuth (from SE to SW), a new coastal reflection secondary microseismic source appears in the northeast part of the bay near the buoy (Fig. 12b). When the swell comes from the SE, the source is more diffuse and seems to be located on a wider range all around the cable with a peak in the northwestern part. As a result, the swell azimuth variations coupled with the geometry of the coastline could explain the different location of the microseismic sources.

By combining the back-projection analysis with the delay between the buoy recordings and the DAS data, we can refine the position of the sources. We focused on two times corresponding to label 1 and label 2 in Fig. 9. In time label 1, the ocean waves travelled in the NW direction and reach first the buoy and then the cable with a 45 min delay. Conversely at time label 2, the waves travelled roughly in the NE direction, reaching the cable first an then the buoy with a 45 min delay. If we assume that gravity waves travel at 15 m s^{-1} over a distance of 25 km between the buoy and the cable section at the coast, the traveltime from the buoy to the coast is 30 min. Similarly, reflected waves will travel 10 km in 15 min. This gives an approximate location of the sources, where the ocean surface gravity waves from opposite directions meet, which we have illustrated with a double grey line in Fig. 12. We are still limited by the approximations in the swell velocities, as well as by the delay of 45 min calculated from the DAS data composed of segments of 8 min every 30 min. These elements show that at least within the 50 km offshore where the cable is located, secondary microseismic

noise sources are located close to the coast (within 15 km), and are strongly influenced by the local gravity wave dynamics.

8 CONCLUSION

This study presents an analysis of secondary microseismic noise coastal sources, using DAS. The DAS measurements are made along a 41.5-km-long dark fibre offshore Toulon, France. The large amount of seismic sensors (more than 2000) along the fibre-optic cable allows us to obtain detailed recordings of ocean surface gravity waves, but also of microseismic noise generated by the interaction between gravity waves and their reflection at the coast.

By comparing data recorded by a marine buoy with the DAS data over a period of 5 d, we were able to attribute the DAS observations to the sea state around the cable. Near the coast, at shallow depths (from 0 to 100 m), the strain produced by gravity waves follows the same dynamics than the significant wave height recorded by the marine buoy. The results of *f–k* analysis and beamforming showed that a fraction (around 30 per cent) of the incident wave trains are reflected at the coast. From the incident and reflected gravity wave ratio, we calculated the reflection coefficient R^2 continuously over a 5-d period. Except when the swell was not intense enough (i.e. below the background noise level) R^2 remained constant around 0.07 over these 5 d. We also showed that R^2 does not change when the wave height varies, but is instead controlled by the ocean wave frequency. This quantification of the reflection coefficient allows to better constrain the reflection of ocean waves and the generation of microseismic sources in numerical models. Farther along the cable and at greater depths (from 1000 to 2500 m), we recorded scattered dispersive Scholte waves which are the secondary microseisms. Spectrogram analysis highlights that the power of the secondary microseisms is correlated with local sea conditions, which indicates that the secondary microseismic is mostly generated near the coast. The *f–k* representations show that, although most of the energy comes from sources near the coast, a small part also comes from more distant sources in open sea. The beamforming results confirm that a large fraction of secondary microseimic sources are located close to the shoreline. In addition, since the coastal reflection sources depend on the frequency characteristics of the waves trains, the occurrence of a new coastal reflection microseismic source requires a certain time which depends on ocean surface gravity waves propagation azimuth. The possibility to monitor and quantify the gravity waves over long distances, their reflection on the coastline and their role in the microseismic source generation from coastal reflection, now appears to be within reach with DAS.

ACKNOWLEDGMENTS

DATA AVAILABILITY

The fibre optic DAS recordings of the microseism signals are available in the following OSF repository: https://osf.io/x6awb/. The WaveWatch model is freely accessible at the IFREMER ftp : ftp.ifremer.fr/ifremer/ww3/HINDCAST.

REFERENCES

Ardhuin, F., Stutzmann, E., Schimmel, M. & Mangeney, A., 2011. Ocean wave sources of seismic noise, *J. geophys. Res.,* **116**(C9), doi:10.1029/2011JC006952.

Ardhuin, F., Balanche, A., Stutzmann, E. & Obrebski, M., 2012. From seismic noise to ocean wave parameters: general methods and validation, *J. geophys. Res.,* **117**(C5), doi:10.1029/2011JC007449.

Bonnefoy-Claudet, S., Cotton, F. & Bard, P.-Y., 2006. The nature of noise wavefield and its applications for site effects studies: a literature review, *Earth-Sci. Rev.,* **79**(3–4), 205–227.

Bromirski, P.D. & Duennebier, F.K., 2002. The near-coastal microseism spectrum: spatial and temporal wave climate relationships, *J. geophys. Res.,* **107**(B8), doi:10.1029/2001JB000265.

Cessaro, R.K., 1994. Sources of primary and secondary microseisms, *Bull. seism. Soc. Am.,* **84**(1), 142–148.

Chang, H. & Nakata, N., 2022. Investigation of time-lapse changes with DAS borehole data at the brady geothermal field using deconvolution interferometry, *Remote Sens.,* **14**(1), doi:10.3390/rs14010185.

Cheng, F., Chi, B., Lindsey, N.J., Dawe, T.C. & Ajo-Franklin, J.B., 2021. Utilizing distributed acoustic sensing and ocean bottom fiber optic cables for submarine structural characterization, *Scient. Rep.,* **11**(1), 5613, doi:10.1038/s41598-021-84845-y.

Deschamps, A. & Beucler, E., 2013. *Posa experiment. resif - réseau sismologique et géodésique français,* doi:10.15778/RESIF.ZH2016.

Elgar, S., Herbers, T.H.C. & Guza, R.T., 1994. Reflection of ocean surface gravity waves from a natural beach, *J. Phys. Oceanogr.,* **24**(7), 1503–1511.

Flores, D.M., Ampuero, J.-P., Mercerat, D., Sladen, A. & Rivet, D., 2021. The potential of DAS on underwater fiber optic cables for deep-sea current monitoring, Tech. rep., Copernicus Meetings.

Goldstein, P. & Archuleta, R.J., 1987. Array analysis of seismic signals, *Geophys. Res. Lett.,* **14**(1), 13–16.

Gualtieri, L., Stutzmann, E., Capdeville, Y., Ardhuin, F., Schimmel, M., Mangeney, A. & Morelli, A., 2013. Modelling secondary microseismic noise by normal mode summation, *J. geophys. Int.,* **193**(3), 1732–1745.

Hasselmann, K., 1963. A statistical analysis of the generation of microseisms, *Rev. Geophys.,* **1**(2), 177–210.

Kedar, S., Longuet-Higgins, M., Webb, F., Graham, N., Clayton, R. & Jones, C., 2008. The origin of deep ocean microseisms in the North Atlantic Ocean, *Proc. R. Soc. A.,* **464**(2091), 777–793.

Koper, K.D., Seats, K. & Benz, H., 2010. On the composition of Earth's short-period seismic noise field, *Bull. seism. Soc. Am.,* **100**(2), 606–617.

Lamare, P., 2016. The MEUST deep sea infrastructure in the Toulon site, *Eur. Phys. J. Conf.,* **116,** doi:10.1051/epjconf/201611609001.

Lamb, H., 1945. *Hydrodynamics,* Dover Publications.

Lindsey, N.J., Dawe, T.C. & Ajo-Franklin, J.B., 2019. Illuminating seafloor faults and ocean dynamics with dark fiber distributed acoustic sensing, *Science,* **366**(6469), 1103–1107.

Lior, I., Mercerat, D.E., Rivet, D., Sladen, A. & Ampuero, J.-P., 2021a. Imaging an underwater basin and its resonance modes using optical fiber distributed acoustic sensing, *Seismol. Res. Lett.,* **93**(3), 1573–1584.

Lior, I. *et al.*, 2021b. On the detection capabilities of underwater distributed acoustic sensing, *J. geophys. Res.,* **126**(3), e2020JB020925, doi:10.1029/2020JB020925.

Longuet-Higgins, M.S., 1950. A theory of the origin of microseisms, *Phil. Trans. R. Soc. Lond., A,* **243**(857), 1–35.

Meng, L., Inbal, A. & Ampuero, J.-P., 2011. A window into the complexity of the dynamic rupture of the 2011 Mw 9 Tohoku-Oki earthquake, *Geophys. Res. Lett.,* **38**(7), doi:10.1029/2011GL048118.

Nishida, K., 2017. Ambient seismic wave field, *Proc. Jpn. Acad., B,* **93**(7), 423–448.

Rivet, D., de Cacqueray, B., Sladen, A., Roques, A. & Calbris, G., 2021. Preliminary assessment of ship detection and trajectory evaluation using distributed acoustic sensing on an optical fiber telecom cable, *J. acoust. Soc. Am.,* **149**(4), 2615–2627.

Schmidt, R., 1986. Multiple emitter location and signal parameter estimation, *IEEE Trans. Antenn. Propagat.,* **34**(3), 276–280.

Sladen, A., Rivet, D., Ampuero, J.-P., De Barros, L., Hello, Y., Calbris, G. & Lamare, P., 2019. Distributed sensing of earthquakes and ocean-solid earth interactions on seafloor telecom cables, *Nat. Commun.,* **10**(1), 1–8.

Spica, Z.J., Nishida, K., Akuhara, T., Pétrélis, F., Shinohara, M. & Yamada, T., 2020. Marine sediment characterized by ocean-bottom fiber-optic seismology, *Geophys. Res. Lett.,* **47**(16), e2020GL088360, doi:10.1029/2020GL088360.

Stehly, L., Campillo, M. & Shapiro, N.M., 2006. A study of the seismic noise from its long-range correlation properties, *J. geophys. Res.,* **111**(B10), doi:10.1029/2005JB004237.

Stutzmann, E., Roult, G. & Astiz, L., 2000. Geoscope station noise levels, *Bull. seism. Soc. Am.,* **90**(3), 690–701.

Stutzmann, E. *et al.*, 2001. Moise: a prototype multiparameter ocean-bottom station, *Bull. seism. Soc. Am.,* **91**(4), 885–892.

Stutzmann, E., Schimmel, M., Patau, G. & Maggi, A., 2009. Global climate imprint on seismic noise, *Geochem. Geophys. Geosyst.,* **10**(11), doi:10.1029/2009GC002619.

Stutzmann, E., Ardhuin, F., Schimmel, M., Mangeney, A. & Patau, G., 2012. Modelling long-term seismic noise in various environments, *J. geophys. Int.,* **191**(2), 707–722.

van den Ende, M. & Ampuero, J.-P., 2021. Evaluating seismic beamforming capabilities of distributed acoustic sensing arrays, *Solid Earth,* **12**(4), 915–934.

Webb, S.C., 1998. Broadband seismology and noise under the ocean, *Rev. Geophys.,* **36**(1), 105–142.

Williams, E.F., Fernández-Ruiz, M.R., Magalhaes, R., Vanthillo, R., Zhan, Z., González-Herráez, M. & Martins, H.F., 2019. Distributed sensing of microseisms and teleseisms with submarine dark fibers, *Nat. Commun.,* **10**(1), 1–11.

SUPPORTING INFORMATION

Supplementary data are available at *GJI* online.

Figure S1. WaveWatch model calculated with the method of Ardhuin *et al*. (2011). Zoom on the Mediterranean sea region on 2 February 2018 at 6 p.m. The DAS is indicated with the red circle. The Balearic Islands are indicated with the black circle.

Please note: Oxford University Press is not responsible for the content or functionality of any supporting materials supplied by the authors. Any queries (other than missing material) should be directed to the corresponding author for the paper.